MATERIALS SCIENCE

Edge-of-chaos learning achieved by ion-electron–coupled dynamics in an ion-gating reservoir

Daiki Nishioka[1,2], Takashi Tsuchiya[1]*, Wataru Namiki[1], Makoto Takayanagi[1,2], Masataka Imura[3], Yasuo Koide[4], Tohru Higuchi[2], Kazuya Terabe[1]

Physical reservoir computing has recently been attracting attention for its ability to substantially reduce the computational resources required to process time series data. However, the physical reservoirs that have been reported to date have had insufficient computational capacity, and most of them have a large volume, which makes their practical application difficult. Here, we describe the development of a Li^+ electrolyte–based ion-gating reservoir (IGR), with ion-electron–coupled dynamics, for use in high-performance physical reservoir computing. A variety of synaptic responses were obtained in response to past experience, which were stored as transient charge density patterns in an electric double layer, at the Li^+ electrolyte/diamond interface. Performance for a second-order nonlinear dynamical equation task is one order of magnitude higher than memristor-based reservoirs. The edge-of-chaos state of the IGR enabled the best computational capacity. The IGR described here opens the way for high-performance and integrated neural network devices.

INTRODUCTION

Artificial neural network (ANN)–based information processing is becoming more and more important as a way to deal with the vast amount of information currently in existence (*1*, *2*). ANN computing [e.g., deep learning with a multilayer neural network (NN)] can provide excellent learning, classification, and inference characteristics that are close to, and in some cases beyond, those found in natural intelligence (i.e., the human brain), whereas the enormous amounts of power required by ANN (as in a typical multilayer NN) are far higher than that required by human beings (*2*). The low-energy efficiency of ANN computing is a serious drawback in the realization of ubiquitous and versatile artificial intelligence (AI) but is inherent in the structure of the ANN, which requires the weights of millions of virtual synaptic nodes to be stored and updated (i.e., large network size) and requires the consumption of tremendous amounts of energy. Reservoir computing (RC) has recently been attracting attention because of its ability to substantially reduce the computational resources required to process time series data, which it is able to do because of its utilization of the nonlinear responses of a "reservoir" to input signals.

While simulated recurrent NNs have been used as reservoirs to perform fully simulated RC (*3*–*5*), materials or devices with nonlinearity, high dimensionality, and short-term memory have been explored as possible "physical reservoirs" that can process information without heavy computational burdens for complicated simulations of the dynamical states of a reservoir (*6*). To date, the nonlinear dynamics of various materials and devices (e.g., soft bodies, optical devices, spin torque oscillators, and memristors) have been reported as providing nonlinear dynamics that are sufficient to perform physical reservoir–based RC with various time series tasks, including image recognition, spoken digit classification, and combinatorial optimization (*6*–*24*). However, to date, the performance of physical reservoir–based RC has been far from satisfactory because of the low expression power of physical reservoirs in comparison to the RC performance of simulated reservoirs. Furthermore, most of the high-performance physical reservoirs have large volumes, more than several cubic centimeters, which are not realistic choices for practical application to integrated AI devices (*7*–*9*). Therefore, achieving compatibility between (i) the high expression power of a physical reservoir and (ii) small reservoir volume is a great challenge in nanotechnology research leading toward the physical implementation of RC at practical levels.

Here, we report the achievement of high-performance physical RC using an ion-gating reservoir (IGR), in which ion-electron–coupled dynamics at a lithium ion electrolyte/diamond interface generate an "edge-of-chaos" state, which is empirically known to exhibit high computational performance (*25*). Various synaptic responses, with asymmetric relaxation and spikes, were obtained with respect to the input history of a single IGR transistor (IGRT), which operates in an electric double layer (EDL) mechanism (*26*–*33*), to achieve excellent expression power in a physical reservoir–based RC. Furthermore, a strong dependence of the synaptic response on channel length, which is a feature of ion-electron–coupled dynamics, is used to realize high dimensionality in a single IGRT. The IGRT exhibited small errors in some RC tasks, including 0.020 of normalized mean squared error (NMSE) in a nonlinear autoregressive moving average (NARMA) task, which is a typical benchmark for RC (*7*, *8*, *13*, *14*, *34*–*37*), and achieved 88.8% accuracy in a handwritten-digit recognition task. The underlying mechanism of the characteristic synaptic response was investigated on the basis of multiphysics simulation, and it was found that complexed charge density patterns form and change from moment to moment in an extremely thin EDL region (<2 nm) during storage and processing of input signals. We further performed a Lyapunov analysis to investigate a possible origin of the high performance from a nonlinear dynamics viewpoint. The calculated value of the maximum Lyapunov exponent was -6.3×10^{-3}, close to an edge-of-chaos

[1]International Center for Materials Nanoarchitectonics (WPI-MANA), National Institute for Materials Science (NIMS), 1-1 Namiki, Tsukuba, Ibaraki 305-0044, Japan. [2]Department of Applied Physics, Faculty of Science, Tokyo University of Science, 6-3-1 Niijuku, Katsushika, Tokyo 125-8585, Japan. [3]Research Center for Functional Materials, NIMS, 1-1 Namiki, Tsukuba, Ibaraki 305-0044, Japan. [4]Research Network and Facility Services Division, NIMS, 1-2-1 Sengen, Tsukuba, Ibaraki 305-0047, Japan.
*Corresponding author. Email: tsuchiya.takashi@nims.go.jp

state, which is located between order ($\lambda < 0$) and chaos ($\lambda > 0$) and is empirically known to derive high expression power from a reservoir in RC (*14*, *22*, *24*, *38*–*40*). Because of the many advantages observed, including (i) the very thin nature of EDL (e.g., nanometer order) and the spontaneous formation at interfaces and (ii) the strong nonlinear response based on ion-electron–coupled dynamics, our approach is useful for realizing high-performance, highly integrated, and low–power consumption AI devices by harnessing the inherent physical and chemical characteristics of materials.

RESULTS AND DISCUSSION

Electrical responses of IGRT and its application to image recognition

In biological neuronal network systems, synaptic responses show characteristic variations in waveform, intensity, and frequency, with respect to environmental inputs in various forms due to the chaotic dynamics of the NN, as illustrated in Fig. 1A (*41*, *42*). The synapses belonging to different dendritic structures are strongly correlated, and their electrical behavior is affected by this correlation. The wide variations in synaptic responses are used to achieve high expression power for efficient information processing. In this study, we use an all-solid-state IGRT, operating in an EDL mechanism, to obtain wide variation in electrical response for efficient information processing. While the versatile electrical behavior in biological neuronal network is due to the correlation between synapses, our IGRT achieves similar versatile electrical responses on the basis of ion-electron–coupled dynamics at a lithium ion electrolyte/diamond interface, as discussed below.

As shown in Fig. 1A, the transistor consists of a lithium ion–conducting solid electrolyte [Li-Si-Zr-O (LSZO)], a hydrogen-terminated diamond (100) single crystal with a homoepitaxial layer, and $LiCoO_2$/Pt gate electrode, which works in the manner of an EDL transistor (EDLT) (*33*). $LiCoO_2$ is a Li^+-electron (hole) mixed conductor, and it serves as the gate electrode by a reversible Li^+ ion insertion/desertion property. It can supply (remove) Li^+ ions

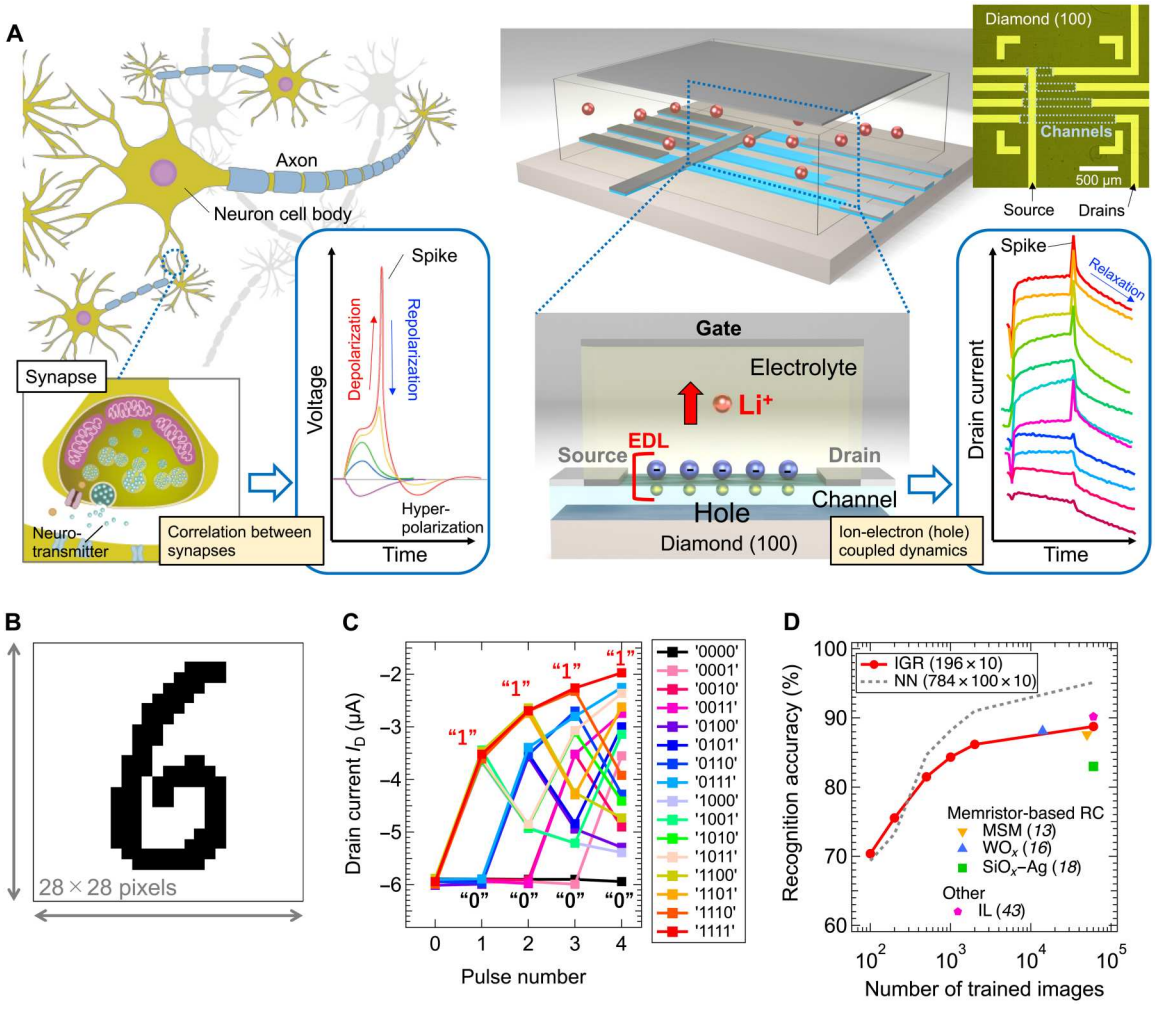

Fig. 1. Electrical response of IGRT based on the EDL effect and its application to image recognition. (**A**) Illustrations of synaptic responses in biological NNs and our IGR operating in an EDL mechanism. (**B**) An example of the handwritten digit 6 from the MNIST database (*44*). (**C**) Drain current (I_D) responses of the IGRT to 16 different pulse streams. (**D**) Image recognition accuracy achieved by IGR as a function of the number of trained images. The dotted line shows the accuracy of a typical, full-simulation, three-layer NN. The size of the IGR and NNs are given in parentheses. The recognition accuracies of other physical reservoirs, such as memristors [magnetic skyrmion memristor (MSM)] (*13*), WO_x (*16*), SiO_x-Ag (*18*), and ionic liquid (IL) (*43*), are shown for comparison.

to (from) the diamond channel/LSZO interface to modulate accumulated charge at the EDL under gate voltage (V_G)–applied conditions. By applying negative V_G to the EDLT, Li^+ ions are removed from the diamond/LSZO interface to form the EDL with negatively charged Li vacancy in the LSZO and positively charged hole in the diamond, resulting in notable conductance enhancement in the channel [a low-resistance state (LRS)], as depicted in Fig. 1A. In the opposite manner, positive V_G application causes Li^+ ion accumulation at the interface, which is accompanied by hole depletion and the resultant insulating [a high-resistance state (HRS)] in the channel. While a transition process from LRS to HRS is fast, the one from HRS to LRS is slow because the Li^+ ion motion in the electrolyte is affected by channel resistance with HRS, that is, the ion-electron–coupled dynamics. The I_D (drain current)–V_G and gate current–V_G curves for IGRT are shown in fig. S1. Details of the dynamics will be discussed later with multiphysics simulation. In

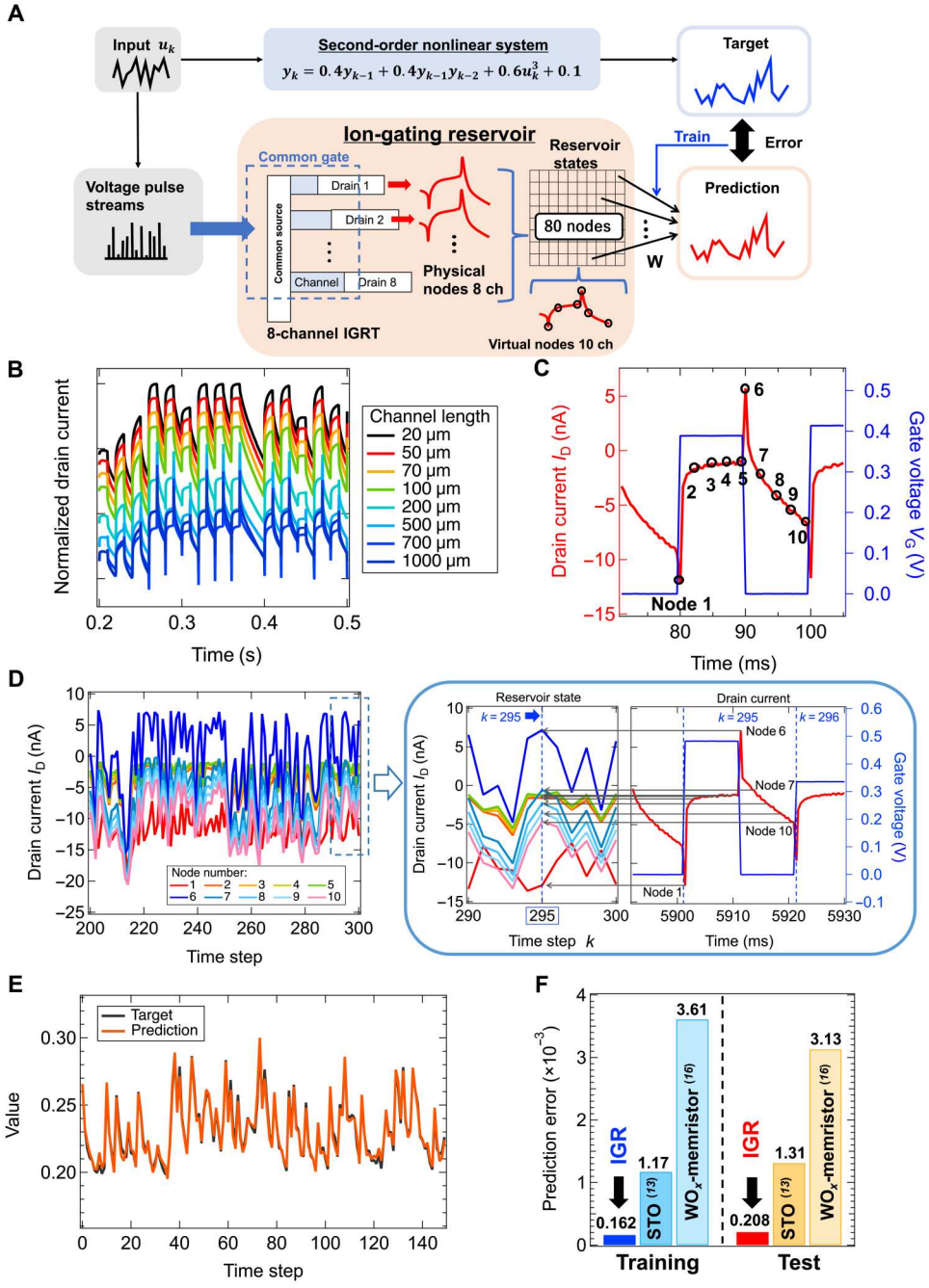

Fig. 2. Solving a second-order nonlinear dynamic equation task. (**A**) Schematic of task calculated by IGR. (**B**) Various I_D responses of the IGRT at different channel lengths. (**C**) The method for obtaining virtual nodes and (**D**) various reservoir states (I_D streams) from 10 virtual nodes. (**E**) Target and prediction waveforms of second-order nonlinear dynamic equation at the test phase. (**F**) Prediction error compared to other physical reservoirs.

addition to the asymmetric relaxation behavior, spikes are observed in the I_D response as shown in Fig. 1A. The spikes are originated from the EDL charging current and useful to enhance diversity of the I_D response, as discussed later. The IGRT has eight channels with different channel length (L). Because all the channels of the device are connected by the electrolyte layer and share common gate and source electrodes, input signals are also shared by the channels. Therefore, the different channels are coupled to each other by three-dimensional Li^+ transport through the electrolyte to some extent.

Said transistor is used as an IGR, which is a novel class of physical reservoirs. The IGR can map time series data in high-dimension feature space by using I_D response, with asymmetric relaxation and spikes, the characteristics of which are widely modified by the input history. To investigate a function of IGR as a physical reservoir, we performed a handwritten-digit recognition task (*13*, *16*, *18*, *43*). Figure 1B is an example of the 28 × 28 pixel input digit "6" from the Modified National Institute of Standards and Technology (MNIST) database (*44*). Said image was converted into binary time series data and input to the IGRT. The reservoir states were obtained from I_D. Figure 1C shows the 16 different reservoir states, which were well separated from each other so that all 16 different pixel combinations could be expressed by unique reservoir states. These values were used as the reservoir output to train and test the readout network. Similar methods have been used elsewhere (*13*, *16*, *18*, *43*). The details of the procedure used are given in Materials and Methods. Figure 1D shows image recognition accuracy versus the number of trained images. The recognition accuracy improved from 70.4 to 88.8% as the number of trained images increased from 100 to 60 thousand, supporting understanding that the recognition task is suitable for the IGR. While the performance was not as good as that achieved by a typical three-layer NN, the size of the network in the present study (1960) is far smaller than in a three-layer NN (784,000). Compared to the recognition accuracies of other physical reservoirs (83 to 90.2%) (*13*, *16*, *18*, *43*), that of IGR is similar or slightly better. However, while the advantage of IGR is minor for such a relatively easy task, IGR showed very good computational performance on more difficult time series data analysis tasks that require superior properties, such as reservoir diversity, which is discussed below.

Solving a second-order nonlinear dynamic equation by IGR

RC is suitable for time series data analysis because it has features such as short-term memory, nonlinearity, and high dimensionality for input data. We took advantage of such suitability by using the IGR to solve a second-order nonlinear dynamical equation task (*13*, *16*), a schematic of which is shown in Fig. 2A. The target $y_t(k)$ is obtained from following equation

$$y_t(k) = 0.4y_t(k-1) + 0.4y_t(k-1)y_t(k-2) + u^3(k) + 0.1 \quad (1)$$

where k and $u(k)$ = [0,0.5] are a discrete time and a random input that were applied to IGRT as V_G pulse streams, respectively. The reservoir states $X_i(k)$ were obtained from the I_D response, and the reservoir output $y(k)$ is the linear combination of $X_i(k)$ and read out weights w_i trained by ridge regression as follows

$$y(k) = \sum_{i=1}^{N} w_i X_i + b \quad (2)$$

where N and b are the reservoir size and bias, respectively. Details of the procedure are given in Materials and Methods.

To obtain high-dimensional reservoir states from one-dimensional input, IGRT with an eight-channel (drain)–one-gate–one-source structure and eight different channel lengths (20 to 1000 μm) were fabricated as shown in Fig. 1A. As shown in Fig. 2A, the eight different channels provide eight physical nodes in the RC. By applying V_G pulse streams to one common gate and one common source, we can measure eight different I_D responses from the eight drains (drains 1 to 8 in Fig. 2A). Constant drain-source voltages (V_D = −500 mV) are applied to between drains 1 and 8 and common source. Concerning V_G pulse streams, a random input $u(k)$ is converted to V_G pulse streams over a range from 0 to 0.5 V (please refer to Materials and Methods for the details). We can get 10 virtual nodes from each of eight different I_D responses. So, we have 80 nodes in total. Target waveform is reproduced from a linear combination of the 80 nodes (reservoir states) with 80 weights. In the training phase, 80 weights are stored in the operating computer, and error was minimized by the ridge regression. Eight I_D responses from common gate inputs were obtained as shown in Fig. 2B. The intensity of the spikes observed at the edges of V_G pulses differ depending on the channel length. The spikes are due to a gate current induced by the ion current, which depends on the differential of charge in the EDL and are more significant with small I_D compared to the gate current. Therefore, short channels with low resistance (≤100 μm) do not exhibit spikes, while long channels with high resistance (≥200 μm) exhibit large spikes. For further higher dimensionality of reservoir states, multiple reservoir states were obtained as virtual nodes, as shown in Fig. 2C (*35*). The former nodes 1 to 5 and the latter nodes 6 to 10 correspond to I_D responses measured during the application of write pulses and during the pulse intervals (V_G = 0 V), respectively. The former nodes use the fast relaxation process of channels from an LRS to an HRS, which is dominated by Li^+ ion accumulation at the electrolyte/channel interface, while the latter nodes use a relaxation process from an HRS to an LRS of the channel, which is a relatively slow relaxation process because the Li^+ ion motion in the electrolyte is affected by channel resistance with HRS. Because of the ion-electron–coupled dynamics, in which the ions of the electrolyte and the electrons of the channel interact, the IGRT exhibits asymmetric relaxation behavior. In addition, nodes 1 and 6 are characteristic virtual nodes located at the peak of the spike-like I_D. Thus, by using the virtual nodes, we could effectively extract features such as asymmetric relaxation and spike behavior, whichare unique features of the EDL. These unique IGR features, induced by ion-electron–coupled dynamics, will be discussed in Fig. 4. Figure 2D shows the reservoir state obtained at each virtual node (1000-μm channel) for a random wave $u(k)$ input. Furthermore, Fig. 2D shows how virtual nodes are taken from the I_D responses measured in the eight physical nodes. One V_G pulse, which corresponds to $u(k)$, gives one I_D response in a physical node just as the one shown in Fig. 2C (80 to 100 ms). It includes 10 virtual nodes as shown in Fig. 2 (C and D). Thus, 10 different I_D streams are reproduced as a function of time step from the 10 virtual nodes as shown in Fig. 2D. Because the device has 8 physical nodes, each of which give 10 virtual nodes, we have 8 (physical nodes) × 10 (virtual nodes) = 80 nodes in total as shown in Fig. 2A. It can be seen that the IGR has good diversity, with each virtual node showing various behaviors as reflections of its own

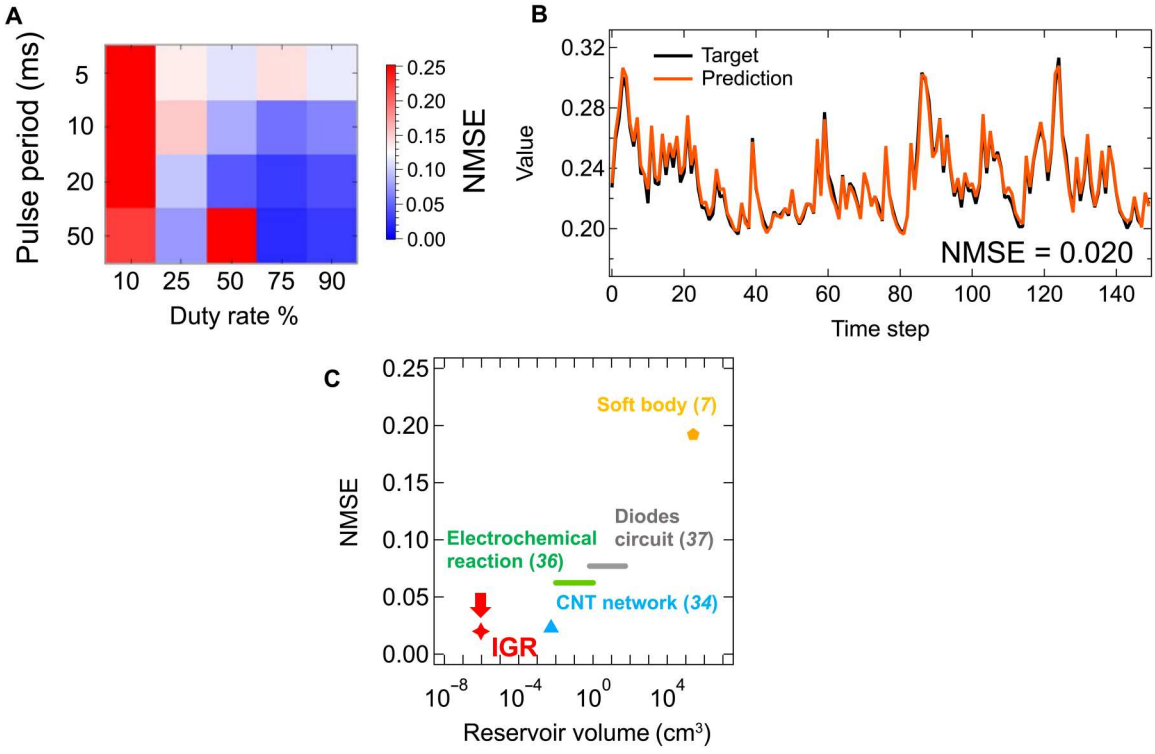

Fig. 3. NARMA2 task. (**A**) The relationship between IGRT operating conditions and NMSEs in the test phase of the NARMA2 task. (**B**) Target and prediction waveforms of the NARMA2 task. (**C**) NMSEs of the NARMA2 task and reservoir volumes of various physical reservoirs, which experimentally demonstrated the NARMA2 task. The reservoir volume of IGR was calculated as the product of the total channel area and the thickness of the electrolyte.

characteristics. The combination of physical and virtual nodes resulted in a reservoir size of 80.

Figure 2E shows the target for the test data and the predicted output by IGR. The predicted output is in excellent agreement with the target, that is, Eq. 1 was successfully solved by the IGR. As shown in Fig. 2F, the predicted error was 1.62×10^{-4} (training data) and 2.08×10^{-4} (test data), respectively. Compared to other physical reservoirs (*13*, *16*), the prediction error was extremely low, indicating that the IGR performs well on time series data analysis tasks. Such good computational performance of IGR is due to its ability to effectively exploit the complex and diverse features inherent in the ion-electron–coupled dynamics of IGR as reservoir states. An additional important factor was the stable reproduction of the good expressivity of the IGR. This means that the nonlinear mapping to higher-dimensional spaces by the IGR performed on the training data was exactly the same as for the test data without altering the IGR condition during operation. This indicates that the IGR satisfies the echo state property, which is one of the important properties required for reservoirs (*3*).

NARMA2 task

We performed predictions on time series data generated by a NARMA2 system (*45*), as shown in Eq. 3, as a more challenging time series data analysis task. This is known as a NARMA2 task and is commonly used as a typical RC benchmark task (*7*, *34*, *36*, *37*).

$$y_t(k+1) = 0.4y_t(k) + 0.4y_t(k)y_t(k-1) + 0.6u^3(k) + 0.1 \quad (3)$$

where $u(k) = [0,0.5]$ is a random input. To evaluate the computational performance of IGR in the NARMA2 task, we used the NMSE for an index of RC performance, an explanation of which is given in Materials and Methods.

Figure 3A shows the relationship between the IGRT operating conditions and the NMSEs (test phase) of the NARMA2 task. Good prediction performance was observed in the operation region with an input pulse period of 20 ms or longer and a duty ratio of 75% or higher. In particular, the best prediction performance (NMSE = 0.020 in the test phase) was achieved at a pulse period of 50 ms and a duty ratio of 75%. The target and the predicted output by IGR (test phase) under these conditions are shown in Fig. 3B. Both waveforms are in excellent agreement, evidencing that IGR successfully predicted the time series generated by the NARMA2 system (please refer to fig. S2 and section S2 for details). Figure 3C shows the relationship between the NMSE of the NARMA2 task in the test phase and the volume of the physical reservoirs reported so far (*7*, *34*, *36*, *37*). Although there are not many reports of physical reservoirs that experimentally demonstrate the NARMA task, IGR showed the best results in the prediction performance despite its extremely small volume compared to other physical reservoirs. That is, the IGR showed both extremely good computational performance on a single device and its suitability for integration. We also evaluated the effect of device geometry on IGR performance. Please refer to fig. S3 and section S3 for details.

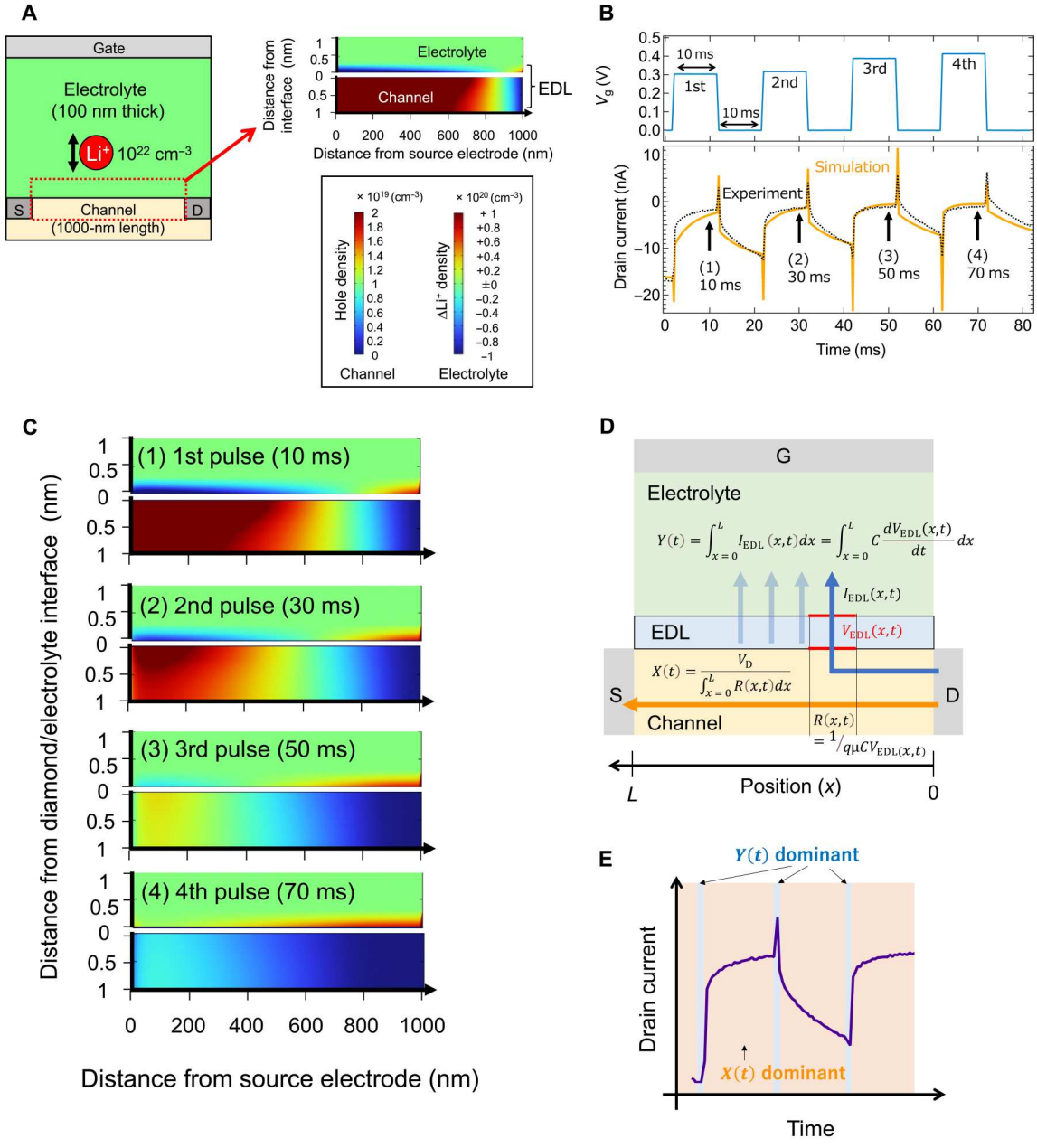

Fig. 4. Simulation of ion-electron–coupled dynamics. (**A**) The simulated EDLT, modeled by COMSOL Multiphysics, and the ion and hole distribution at the electrolyte/channel interface at the initial state. The ion distribution of the electrolyte shows the amount of change from 10^{22} cm^{-3} of Li^+ concentration. (**B**) The I_D response of the simulated model under sequential gate pulse applied condition. The dotted line shows the experimental result. (**C**) Snapshots of the ion and hole distribution, which are captured at each of the four pulses shown in (B). (**D**) Schematic illustration of the I_D path in the IGR, consisting of two I_Ds: one corresponding to state variable $X(t)$ and the other corresponding to state variable $Y(t)$. (**E**) The I_D response as a mixed reservoir of $X(t)$ and $Y(t)$.

Simulation of ion-electron–coupled dynamics in IGR

The ion and electron dynamics in our IGR were simulated by using COMSOL multiphysics simulation software (COMSOL Inc.) to clarify the underlying mechanism in the unique *I*-*V* characteristics of our device. As shown in Fig. 4A, the EDLT model, which is composed of a Li^+ electrolyte, a channel, and electrodes, was constructed by assuming the physical properties of LSZO, EDL, and the device structure with an adjustment of for reduction of computation burden. The I_D-V_G and I_D-V_D characteristics of the simulated model agreed well with the experimental result (please refer to fig. S4, A and B, and to Materials and Methods). Figure 4B shows the I_D response of the device model under four sequential gate pulse applied conditions. As seen in the rise and fall behavior of I_D, the model reproduces asymmetric I_D responses with spikes that are signatures of our device, supporting our understanding that the simulation reproduces the actual electrochemical transport phenomena in the device. To grasp the ion and electron (hole) dynamics in the model in the operation, we capture snapshots of the ion and hole

density distribution at specific points. In the snapshot at the initial state, shown in Fig. 4A, substantial in-plane carrier distribution is found, in which densities of positively charged holes and negatively charged Li vacancies are higher near the source electrode than near the drain electrode. This corresponds to formation of EDL, which is differently charged by voltage distribution due to application of V_D (= − 500 mV) between the source and drain electrodes. It is noted that the out-of-plane distribution of excess Li^+ (and Li vacancies) accumulates within 0.3 nm from the interface. The extremely thin nature of the EDL is consistent with the in situ hard x-ray photoelectron spectroscopy observation (*33*). Besides, comparison between the four conditions shown in Fig. 4C evidences that repetition of input makes a variety of charge density patterns in the channel. For example, at t = 50 ms, not only the low–hole density region proceeds from the drain side to the source side; an island-like pattern also appears within 0.3 nm from the channel/electrolyte interface. This is because such proceeding of the low–hole density region occurs not only from the drain side but also from the source side, resulting in a variety of transient charge density patterns. Please refer to movie S1 and fig. S5 for a movie of the charge density variation and a detailed discussion on the charge distribution change for the first pulse input, respectively.

Basically, such behavior can be understood in the framework of transmission line model, in which electrical resistance is dependent on the location due to the different length of the current path (*46*). However, in the present case, local hole resistance in the channel is strongly dependent on the charging history of EDL. This gives the I_D response of the IGR asymmetric relaxation. Furthermore, spikes add another feature to the response. High performance of the IGR is discussed below as two contributions to the total I_D: I_D to the source and I_D to the gate. Figure 4D is an illustration of the I_D path in the IGR. A partial I_D (from the drain to source) corresponds to state variable $X(t)$ defined with an integral of local resistance $R(x,t)$ at each channel position x ($0 \le x \le L$), $X(t) = \frac{V_D}{\int_{x=0}^{L} R(x,t)\,dx}$, in which L, x, and V_D are channel length, position in the channel, and drain voltage (constant), respectively. By introducing a local voltage applied to EDL V_{EDL} (x,t) and EDL capacitance (constant) C, $X(t)$ can be further transformed to

$$X(t) = \int_{x=0}^{L} V_D q\mu C V_{EDL}(x,t)\,dx \quad (4)$$

in which q and μ are the elementary charge and hole mobility, respectively. On the other hand, the rest of the I_D with a spike appearance (from the drain to the gate) corresponds to state variable $Y(t)$, defined with an integral of EDL charging current I_{EDL} (x,t) at each channel position x ($0 \le x \le L$)

$$Y(t) = \int_{x=0}^{L} I_{EDL}(x,t)\,dx = \int_{x=0}^{L} C\frac{dV_{EDL}(x,t)}{dt}\,dx \quad (5)$$

in which $V_{EDL}(x,t)$ and C are a local voltage applied to EDL and EDL capacitance (constant), respectively. As seen from Eqs. 4 and 5, while both $X(t)$ and $Y(t)$ include $V_{EDL}(x,t)$, it is only expressed in a derivative form. Therefore, although both $X(t)$ and $Y(t)$ are related to $V_{EDL}(x,t)$, they function as two different types of reservoir. Because the I_D observed is the sum of I_D to source and to gate, the I_D response is a mixed reservoir of $X(t)$ and $Y(t)$, as shown in Fig. 4E. Recently, such mixed reservoirs have been theoretically predicted to show high performance by overcoming a trade-off relationship between short-term memory and nonlinearity due to the coexistence or mixture of linear dynamics and nonlinear dynamics in a reservoir (*47*). The mixed reservoir property can be a reasonable explanation for the high performance discussed in time series data analysis tasks shown in Figs. 2 and 3. In addition, we evaluated the virtual node dependence of NMSE for NARMA2 task to analyze the mixed reservoir effect in IGR. The best prediction performance was obtained for virtual nodes 1 and 6, which correspond to the spike behavior of the I_D ($Y(t)$ dominant regions in Fig. 4E), as shown in fig. S6A. This indicates that such spikes not only provide reservoir diversity shown in fig. S6B but also contribute significantly to the computation. Please refer to section S5 for detailed discussion.

Lyapunov analysis

To evaluate the high performance of the IGR in terms of nonlinear dynamics, we calculated the Lyapunov exponent, which quantifies the trajectory stability of the dynamical system by the Jacobi matrix method for direct analysis of time series data based on unknown dynamical systems (*39*, *48*). Figure 5A shows the nonlinear I_D response used in the chaos time series analysis for the 20-, 700-, and 1000-μm channels when a triangular wave is input to the IGRT. These channels exhibit completely different nonlinear responses, including the presence of spikes. While I_D response for L = 20 μm shows monotonical increase (blue arrow) and decrease (red arrow) with respect to the input triangle waves, those for L = 700 μm and L = 1000 μm show much complex behavior with negative differential resistance–like nonlinear input-output characteristics. Specifically, the I_D responses for L = 700 μm and L = 1000 μm show a decrease in I_D output as indicated by blue arrows in regions where input V_G increases (colored in red in the inset) and an increase in I_D output as indicated by red arrows in regions where input V_G decreases (colored in blue in the inset). Such a negative differential resistance–like nonlinear input-output characteristic is a highly nonlinear behavior that has been reported for memristors in edge-of-chaos states (*49*). To analyze the nonlinearity of IGR in detail, we generated 40 reservoir states X by obtaining five virtual nodes, corresponding to nodes 1 to 5 in Fig. 2C, for I_D obtained from eight channels.

Figure 5B shows the return map [$X(k)$ versus $X(k + 1)$] obtained from the reservoir states of nodes 1 and 5 with L = 20 μm, L = 700 μm, and L = 1000 μm ($X_{20\mu m,Node1}$, $X_{20\mu m,Node5}$, $X_{700\mu m,Node1}$, $X_{700\mu m,Node5}$, $X_{1000\mu m,Node1}$, and $X_{1000\mu m,Node5}$). The return maps are completely different for each virtual node and for each channel length (physical node), which indicates that IGR achieves good diversity as a result of higher dimensioning by introducing virtual node and channel length. The return map at L = 20 μm, shown on the left of Fig. 5B, has a narrow trajectory width, indicating an almost completely periodic response to the triangular wave input. On the other hand, the return map at L = 700 μm and L = 1000 μm, shown in the middle and right of Fig. 5B, has a wide trajectory, indicating that the reservoir state has a relatively unstable response that varies slightly from period to period. Similar unstable characteristics have been reported for memristors (*49*) and nanowire networks (*22*) in chaos and edge-of-chaos states. We calculated Lyapunov exponents λ, an index of order-chaotic dynamics, of the IGR using the Jacobi matrix method (*39*, *48*). Figure 5C shows the attractor in phase space created by selecting

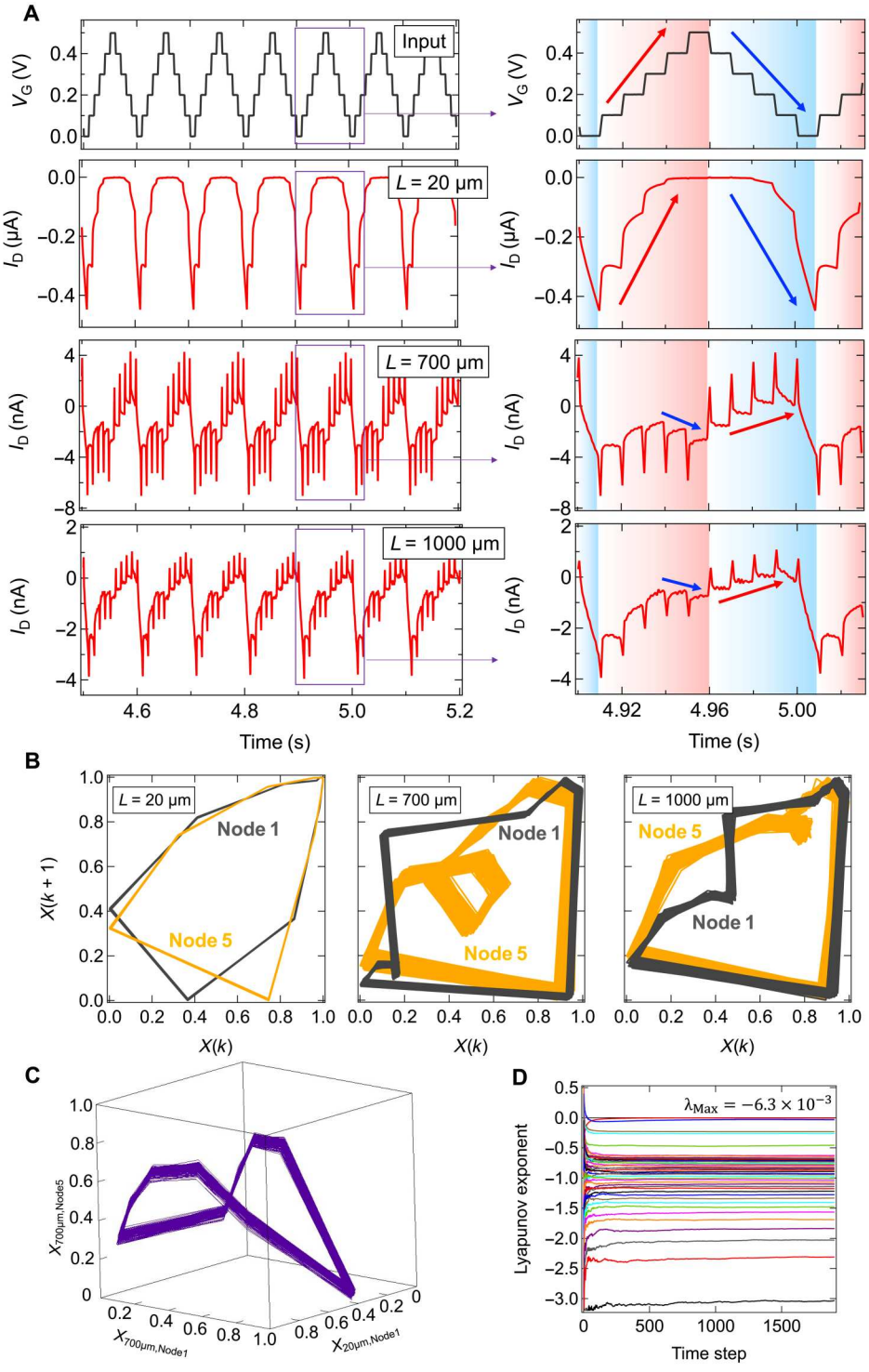

Fig. 5. Lyapunov analysis. (**A**) Nonlinear I_D response of the IGR. Triangular wave input (top) and I_D response of IGR obtained from 20-μm length channel, 700-μm length channel, and 1000-μm length channel. (**B**) The return maps of the reservoir correspond to a 20-μm length channel (left), a 700-μm length channel (middle), and a 1000-μm length channel (right) with nodes 1 and 5. (**C**) The three-dimensional cross section of the 41D reservoir state spaces of the IGR. (**D**) Lyapunov spectrum of the IGR calculated by the Jacobi matrix method.

the axes in the $X_{20\mu m,Node1}$, $X_{700\mu m,Node1}$, and $X_{700\mu m,Node5}$ directions as one of the cross sections of the 41-dimensional phase space. The calculated Lyapunov spectrum is also shown in Fig. 5D. The Lyapunov exponents show values ranging from a minimum of −3.0 to a maximum of -6.3×10^{-3}: The maximum Lyapunov exponents λ_{Max} of the IGR is -6.3×10^{-3}. Dynamical systems with maximum Lyapunov exponents λ_{Max} near zero are called edges of chaos, and it has been reported that high computational performance is achieved at these edges of chaos in computing for physical reservoirs (*14*, *22*, *24*), full simulation reservoirs (*38*–*40*), and recurrent NN (*50*) because of their robustness in the processing of information (*25*). The high computational performance of IGR can also be attributed to edge of chaos, which was achieved by nonlinearity and high dimensionality. In other words, the high expressivity is realized by the asymmetric relaxation and spiking of the I_D, which originates from the ion-electron–coupled dynamics at the electrolyte/semiconductor interface.

During application of pulse V_G streams to the IGRT, diverse and complex charge density distribution is formed by reflecting the past experience (hysteresis) as discussed in Fig. 4. Because of ion-electron–coupled dynamics, ionic and electronic carrier density distributions at a certain time step k strongly affect on the carrier density distributions formed by subsequential applications of V_G pulse streams later than time step $k + 1$. Therefore, the carrier density distribution becomes very sensitive to the past experience, and it gives instability to the system, leading to the edge-of-chaos state.

To achieve high-performance RC, we developed an IGR on the basis of ion-electron–coupled dynamics in the vicinity of a lithium ion solid electrolyte/diamond interface. In the study, various synaptic responses, with asymmetric relaxation and spikes, are effective in achieving excellent expression power for mapping time series data to higher-dimensional feature space. Good RC performance of the IGR was demonstrated in handwritten-digit recognition, nonlinear transformations, and NARMA2 tasks. Multiphysics simulation revealed that during operation, transient charge density patterns form and change from moment to moment in an extremely thin EDL region. Asymmetric relaxation and spikes in the I_D response enables high expression power by realizing a mixed reservoir comprising different nonlinear dynamics. Lyapunov analysis was performed to inspect the dynamical features of the IGR, which analysis revealed that the maximum Lyapunov exponents of the carrier dynamics is -6.3×10^{-3}, supporting the understanding that the IGR operates in edge-of-chaos states under certain conditions. Furthermore, the concept of an IGR can be extended to various information carriers (e.g., electrons, ions, light, and spin) as long as their dynamics or transport interact with each other. While the present EDL system, with its ion-gating transistor structure, is a typical case, various physical or chemical systems can be used for achieving IGR with diverse information carriers. Various materials and interfaces present exciting frontiers for exploring high-performance, versatile, and integrated physical RC based on the coupled dynamics inherent in IGR.

MATERIALS AND METHODS

Device fabrication

Hydrogen-terminated diamond was deposited on a single crystal diamond substrate (100) (EDP) by the microwave-plasma chemical vapor deposition (MPCVD) method. During deposition, 500 and 0.5 standard cubic centimeter per minute of H_2 and CH_4, respectively, were introduced, and the hydrogen-terminated diamond was grown at 950-W radio frequency power. The IGRT were fabricated with eight different channel lengths (20, 50, 70, 100, 200, 500, 700, and 1000 μm), all with a channel width of 100 μm. Pd/Pt electrodes (10 and 35 nm, respectively) were deposited by electron beam evaporation with maskless lithography after oxygen termination of the diamond surfaces, other than channels, by oxygen plasma asher. A 3.5-μm LSZO thin film, used as an electrolyte, was deposited by pulsed laser deposition (PLD) with an ArF excimer laser. $LiCoO_2$ (100 nm) was deposited by PLD to form the gate electrode, and a 50-nm Pt thin film was deposited by electron beam deposition.

Note that encapsulation technology has been well established for fabrication of integrated circuits (ICs) in commercial electronic devices (*51*) Transfer molding and compression molding using various types of resin (semiconductor encapsulant) are widely used to keep ICs in vacuum to protect them. In addition, materials in our devices were so stable that we could fabricate our devices in air, although we performed electrical measurements in vacuum for keeping our devices in the best condition. Therefore, there is no severe limitation to practical applications.

Measurement method

IGRT measurements were carried out at room temperature in a vacuum chamber evacuated by a turbo molecular pump. Probers were used to connect the IGRT in the chamber, and electrical measurements were performed using the source measure unit and pulse measure unit of a semiconductor parameter analyzer (4200A-SCS, Keithley).

Image recognition

A handwritten digit from the MNIST dataset (*44*) was used for the task of image recognition by IGR, with 60,000 images as training data and 10,000 as test data. Each pixel of a 28 × 28 pixel handwritten digit was converted to a binary state of "0" or "1" and input to the IGRT as a time series data signal every 4 pixels. The "0" and "1" were set to $V_G = -0.5$ V and $V_G = 0.3$ V, respectively, and the pulse widths were 10 ms for each. The pulse interval was set to 12.5 ms, and $V_G = -0.5$ V was also applied during this time. While measuring the I_D by applying a constant drain voltage ($V_D = -0.5$ V) to the IGRT, 16 different time series data ("0000" to "1111") were input to the IGRT, and an I_D of 12.5 ms after the fourth pulse input was obtained as the reservoir state. The 16 I_Ds obtained by the measurements were normalized so that the I_D corresponding to "1111," which has the largest value, became 1 after adding 6 μA as an offset to the I_D. Then, the 784-pixel digit data were replaced with the reservoir state every 4 pixels, and the digit data converted to 196 values of reservoir state were trained and classified in the readout network. With the reservoir state matrix as $\boldsymbol{X}$ and the weight matrix of the readout network as $\boldsymbol{W}$, the readout function is defined as follows

$$h(X) = g(\boldsymbol{W} \cdot \boldsymbol{X}) \tag{6}$$

$$g(z) = \frac{1}{1 + e^{-z}} \tag{7}$$

The squared error is defined as

$$E = \frac{1}{2}\sum_{i=1}^{10}[y_i - h(x_i)]^2 \quad (8)$$

The weights W were updated to minimize

$$\Delta W = -\alpha\frac{\partial E}{\partial W} \quad (9)$$

The learning rate α was set to 0.1, and the training was performed 20 times.

Solving second-order nonlinear dynamic equation tasks

A random input $u(k)$ was converted to voltage pulse streams, with a pulse width of 10 ms and an interval of 10 ms, and applied to the gate terminal of the IGRT. The intensity of the pulses $V_G(k)$ was equal to $u(k)$, over a range of 0 to 0.5 V, and V_G = 0 V was applied during pulse intervals. The I_D responses of the IGRT with eight channels were measured under constant V_D = −0.5 V, and 10 virtual nodes were obtained from each of them. Thus, 80 reservoir states were obtained from one-dimensional input $u(k)$ by IGR. These reservoir states were normalized from 0 to 1 for calculation, as shown in Eq. 2.

Ridge regression for solving second-order nonlinear dynamic equation tasks and NARMA2 tasks

In the time series data analysis tasks shown in Figs. 2 and 3, the readout network of IGR was trained by ridge regression. Here, we explain the algorithm for ridge regression. The reservoir output $y(k)$ shown in Eq. 2 is transformed to

$$y(k) = \boldsymbol{W}\cdot\boldsymbol{x}(k) \quad (10)$$

where $\boldsymbol{W} = (w_0, w_1,...w_N)$ and $\boldsymbol{x}(k) = [X_0(k), X_1(k),..., X_N(k)]^T$ are the weight vector and the reservoir state vector with a reservoir size of N, respectively. Note that $w_0 = b$ and $X_0(k) = 1$ to introduce the bias b shown in Eq. 2. The cost function $J(\boldsymbol{W})$ in ridge regression is defined as follows

$$J(\boldsymbol{W}) = \frac{1}{2}\sum_{k=1}^{T}[y_t\ (k) - y(k)]^2 + \frac{\lambda}{2}\sum_{i=0}^{N}w_i^2 \quad (11)$$

where T, λ, and $y_t(k)$ are the data length in the training phase, the ridge parameter, and the target output generated by Eq. 1 or 3, respectively. We fixed T = 450 and λ = 5×10^{-4} for all the tasks demonstrated in Figs. 2 and 3. The weight matrix $\widehat{\boldsymbol{W}}$ that minimizes cost function $J(\boldsymbol{W})$ is given by following Eq. 12

$$\widehat{\mathbf{W}} = \boldsymbol{Y}\boldsymbol{X}^T(\boldsymbol{X}\boldsymbol{X}^T + \lambda\boldsymbol{I})^{-1} \quad (12)$$

where $\boldsymbol{Y} = [y_t(1), y_t(2),..., y_t(T)]$, $\boldsymbol{X} = [\boldsymbol{x}(1), \boldsymbol{x}(2),..., \boldsymbol{x}(T)]$, and $\boldsymbol{I}[\subseteq \mathbb{R}^{(N+1)\times(N+1)}]$ are the target output vector, the reservoir state matrix, and the identify matrix, respectively.

Then, after learning the readout weights, the computational performance was evaluated by "Prediction error" for solving the second-order nonlinear dynamic equation task and "NMSE" for the NARMA2 task, as shown in following Eqs. 13 and 14

$$\text{Prediction error} = \frac{\sum_{k=1}^{T}[y_t(k) - y(k)]^2}{\sum_{k=1}^{T}y_t^2(k)} \quad (13)$$

$$\text{NMSE} = \frac{1}{T}\frac{\sum_{k=1}^{T}[y_t(k) - y(k)]^2}{\sigma^2[y_t(k)]} \quad (14)$$

where T is a data length in the training phase (T = 450) or test phase (T = 150).

Multiphysics modeling

To analyze the dynamical behavior of ions and electrons in IGRT, finite element modeling and simulation of IGRT was performed with the COMSOL Multiphysics (COMSOL Inc.). So far, there have been many reports on such simulations of field-effect transistors and also EDL capacitors (*52*–*56*). On the basis of the approaches in the literatures, our IGRT model was constructed by modifying the main framework of a conventional field-effect transistor model comprising a semiconductor channel, electrodes (source, drain, and gate), and gate dielectric (*52*, *53*). By modifying the conventional field-effect transistor model with (i) insertion of an ion-conducting electrolyte layer between semiconductor channel and gate electrode to form the semiconductor channel/gate dielectric/electrolyte layer/gate electrode–laminated structure and (ii) assuming the gate dielectric as EDL with constant and huge capacitance, semiconductor channel, we made our IGRT model in which EDL charging/discharging modulate the semiconductor channel resistance.

In the semiconductor channel corresponding to the diamond channel in the IGRT, we applied a standard description of electronic carrier transport in semiconductor by using Poison equation describing the relationship between electric potential (Ψ) and electric charge density (ρ) as shown in Eq. 15 and semiconductor equations as shown in Eqs. 16 and 17 (*52*, *53*). To lower computation burden, only major hole transport was simulated by ignoring minor electron transport.

$$\nabla\cdot(-\nabla\Psi) = \frac{\rho}{\varepsilon}, \rho = q(\rho - N_a^-) \quad (15)$$

where ε, p, and N_a^- are the permittivity, carrier concentrations of holes, and acceptor concentrations, respectively.

$$J_p = -qD_p\nabla p - qn\mu_p\nabla\Psi \quad (16)$$

$$\frac{\partial p}{\partial t} = \left(\frac{1}{q}\right)\nabla\cdot J_p - \frac{\Delta p}{\tau} \quad (17)$$

where J_p and τ are the hole current densities and the hole lifetime, respectively. D_p and μ_p are the hole diffusion coefficient and mobility, respectively, satisfying the following Einstein relation

$$\mu_p = \frac{q}{k_B T}D_p \quad (18)$$

where q, k_B, and T are the elementary charge (1.60×10^{-19} C),

Boltzmann constant (1.38×10^{-23} J/K), and room temperature (293.15 K), respectively. In our model, we used the experimental result of 150 cm^2/Vs for the hole mobility (*33*). As for the carrier density of the diamond channel, high-density H-termination (10^{13} cm^{-2}) on the surface of the diamond was reported to cause the two-dimensional hole gas on the surface of diamond (*57*). To approximate the two-dimensional hole gas, 10^{19} cm^{-3} was set for acceptor concentration by considering H-termination density (10^{13} cm^{-2}) and thickness of the two-dimensional hole gas (1 nm) (*58*). As seen in fig. S4, I_D-V_G and I_D-V_D characteristics of the diamond-based IGRT were successfully reproduced, indicating that the hole transport property on the surface of H-terminated diamond was approximated with sufficient accuracy for the present study.

In the electrolyte layer corresponding to LSZO in our IGRT, Li^+ transport is described by Nernst-Planck equation in which ion flux J_i is a sum of diffusion flux J_{diff} and drift flux J_{drift} as follows

$$J_i = J_{diff} + J_{drift} = -D\nabla c - c\mu_i \nabla \Psi \tag{19}$$

where D, c, and μ_i are diffusion coefficient, ion concentration, and the ion mobility, respectively. Our model describes Li^+ transport in the electrolyte by solving the Nernst-Planck equation. Li^+ carrier density was set to 10^{22} cm^{-3} by using Li concentration in our LSZO investigated by inductively coupled plasma mass spectroscopy. There have been only few reports on mobility and diffusion coefficient of Li^+ conducting amorphous inorganic oxide films, and we could not find the values for LSZO film (*59*). We thus substituted diffusion coefficient of Li^+-conducting Li_3PO_4 amorphous films for the one of LSZO. Therefore, we calculated mobility of the electrolyte in the IGRT model from diffusion coefficient of Li_3PO_4 amorphous films (6.3×10^{-13} cm^2/s) (*59*). In our IGRT model, the electrolyte layer was divided by a triangular mesh, which was designed to keep the maximum mesh size below 0.18 nm in the region within a distance of 2.5 nm from the diamond/EDL interface, in which drastic variation in carrier density is expected. On the other hand, outside of the region, the mesh size was designed to be less than 20 nm to reduce computational burden.

As for the gate dielectric corresponding to EDL, the capacitance C_{EDL} was set to 4.0 μF/cm^2, which is a typical value of EDL capacitance. To express EDL with capacitance C_{EDL} = 4.0 μF/cm^2 in Helmholz model (*54*–*56*), thickness (d) and dielectric constant (ε_r) of the gate dielectric were set to 1 nm and 4.5 based on the relationship $C_{EDL} = \varepsilon_0 \varepsilon_r / d$. While we observed V_G dependence of EDL capacitance at diamond/LSZO interface (*33*), it was simplified to constant capacitance. As shown as the Eq. 5 in the discussion for reservoir state $Y(t)$, EDL charging/discharging current density J_{EDL} is expressed by following Eq. 20, which relates to the modulation of the channel resistance caused by EDL charging/discharging in our IGRT model (*56*).

$$J_{EDL} = C_{EDL} \frac{d(\Psi_{ch} - \Psi_{el})}{dt} \tag{20}$$

where Ψ_{ch} and Ψ_{el} are the electric potential at the diamond channel and electrolyte, respectively.

Our IGRT model consists of a Li^+ electrolyte, EDL, and diamond channel and was modeled in two dimensions. In the EDL charging process, Li^+ ion transport in the LSZO electrolyte contribute as a serial resistance to the whole electrical system. The serial resistance R for the Li^+ ion transport is derived from Li^+ ion conductivity, $\sigma = (q)^2 nD/k_B T$, and geometric configuration [thickness (t) and channel length (L)] of the electrolyte, by considering that R is in inversely proportion to both t and L. Here, n and T are carrier density and temperature, respectively. For reducing of the system volume by maintaining R. To reduce computational burden, the simulation model reduces the channel length from 20 to 1000 μm in the real device to 1000 nm and reduces the electrolyte thickness from 3.5 μm in the real device to 100 nm. The diffusion coefficient of the Li^+ electrolyte was reduced from 6.3×10^{-13} to 10^{-14} cm^2/s, and the mobility of Li^+ was set to 4×10^{-13} cm^2/Vs to maintain ionic resistance with decreasing size and in good agreement with the experimental results. The boundary condition at the bottom of the channel (substrate side) was set to the insulator. The source, drain, and gate electrodes were modeled as ohmic contacts. A potential of 0 V is set on the source electrode. Drain and V_G are applied to the electrodes with respect to the source electrode.

Lyapunov analysis

Here, we introduce how the Lyapunov exponents of IGR were calculated by the Jacobi matrix method (*39*, *48*, (*60*). The Jacobi method matrix estimates the Jacobi matrix from points on the attractor in the m-dimensional phase space of the time series data. Let us consider an m-dimensional sphere (ε sphere) of infinitesimal radius ϵ, centered at a point $\boldsymbol{v}(t)$ on the orbit of the attractor at time t. With $\boldsymbol{v}(k_i)$ (i = 1, 2,..., M) as the other points on the attractor located inside the ε sphere, the displacement vector $\boldsymbol{\mu}_i$ of $\boldsymbol{v}(k_i)$ as seen from $\boldsymbol{v}(t)$ is obtained as follows

$$\boldsymbol{\mu}_i = v(k_i) - v(t) \tag{21}$$

In addition, the displacement vector $\boldsymbol{z}_i$ after time s is obtained as follows, and a small radius of ε sphere and s allows a linear approximation shown on the right of the equation as $\widehat{\boldsymbol{J}}(t)$, which is the Jacobi matrix to estimate

$$Z_i = v(k_i + s) - v(t + s) \approx \widehat{\boldsymbol{J}}(t)\boldsymbol{\mu}_i \tag{22}$$

Then, from Eq. 22, the Jacobi matrix can be estimated as follows

$$\widehat{\boldsymbol{J}}(t) = z_i \boldsymbol{\mu}_i^T (\boldsymbol{\mu}_i \boldsymbol{\mu}_i^T) \tag{23}$$

Considering the QR decomposition of the Jacobi matrix, the Jacobi matrix at time t can be expressed as shown in Eq. 24, and the Lyapunov exponent λ_i for i = 1, 2,..., m is calculated as shown in Eq. 25

$$\widehat{\boldsymbol{J}}(t)\ Q_t = Q_{t+1}\ R_{t+1} \tag{24}$$

$$\lambda_i = \lim_{T \to \infty} \frac{1}{2T} \sum_{k=1}^{2T} \log \mid R_k^{ii} \mid \tag{25}$$

where R_k^{ii} is the ith diagonal element of the upper triangular matrix $\boldsymbol{R}_k$.

Whereas the Lyapunov exponent λ_i is ideally defined by a limit of Eq. 25 as a time step k goes infinite, it is analytically calculated from experimental data with finite points. Therefore, the calculated Lyapunov exponents become reliable only when the values are sufficiently converged. On the other hand, in the very initial time steps near zero, the Lyapunov exponents are not converged, thus,

deviating largely. That is why we observe very large positive or negative Lyapunov exponents in the near zero region ($k \approx 0$). In Fig. 5D, we can safely conclude that the Lyapunov exponents are sufficiently converged in $k > 1500$.

Supplementary Materials

This PDF file includes:
Sections S1 to S5
Figs. S1 to S6

Other Supplementary Material for this manuscript includes the following:
Movie S1

REFERENCES AND NOTES

1. Y. LeCun, Y. Bengio, G. Hinton, Deep learning. *Nature* **521**, 436–444 (2015).
2. C. C. Aggarwal, *Neural Networks and Deep Learning* (Springer, 2018).
3. H. Jaeger, The "echo state" approach to analysing and training recurrent neural networks with an erratum note (German National Research Center for Information Technology GMD Technical Report, 2001), vol. 148, p. 13.
4. H. Jaeger, H. Haas, Harnessing nonlinearity: Predicting chaotic systems and saving energy in wireless communication. *Science* **304**, 78–80 (2004).
5. W. Maass, T. Natschläger, H. Markram, Real-time computing without stable states: A new framework for neural computation based on perturbations. *Neural Comput.* **14**, 2531–2560 (2002).
6. G. Tanaka, T. Yamane, J. B. Héroux, R. Nakane, N. Kanazawa, S. Takeda, H. Numata, D. Nakano, A. Hirose, Recent advances in physical reservoir computing: A review. *Neural Netw.* **115**, 100–123 (2019).
7. K. Nakajima, H. Hauser, T. Li, R. Pfeifer, Information processing via physical soft body. *Sci. Rep.* **5**, 10487 (2015).
8. Y. Paquot, F. Duport, A. Smerieri, J. Dambre, B. Schrauwen, M. Haelterman, S. Massar, Optoelectronic reservoir computing. *Sci. Rep.* **2**, 287 (2012).
9. G. Van der Sande, D. Brunner, M. C. Soriano, Advances in photonic reservoir computing. *Nanophotonics* **6**, 561–576 (2017).
10. J. Torrejon, M. Riou, F. A. Araujo, S. Tsunegi, G. Khalsa, D. Querlioz, P. Bortolotti, V. Cros, K. Yakushiji, A. Fukushima, H. Kubota, S. Yuasa, M. D. Stiles, J. Grollier, Neuromorphic computing with nanoscale spintronic oscillators. *Nature* **547**, 428–431 (2017).
11. R. Nakane, G. Tanaka, A. Hirose, Reservoir computing with spin waves excited in a garnet film. *IEEE access* **6**, 4462–4469 (2018).
12. S. Tsunegi, T. Taniguchi, K. Nakajima, S. Miwa, K. Yakushiji, A. Fukushima, S. Yuasa, H. Kubota, Physical reservoir computing based on spin torque oscillator with forced synchronization. *Appl. Phys. Lett.* **114**, 164101 (2019).
13. W. Jiang, L. Chen, K. Zhou, L. Li, Q. Fu, Y. Du, R. H. Liu, Physical reservoir computing using magnetic skyrmion memristor and spin torque nano-oscillator. *Appl. Phys. Lett.* **115**, 192403 (2019).
14. N. Akashi, T. Yamaguchi, S. Tsunegi, T. Taniguchi, M. Nishida, R. Sakurai, Y. Wakao, K. Nakajima, Input-driven bifurcations and information processing capacity in spintronics reservoirs. *Phys. Rev. Res.* **2**, 043303 (2020).
15. H. O. Sillin, R. Aguilera, H. H. Shieh, A. V. Avizienis, M. Aono, A. Z. Stieg, J. K. Gimzewski, A theoretical and experimental study of neuromorphic atomic switch networks for reservoir computing. *Nanotechnology* **24**, 384004 (2013).
16. C. Du, F. Cai, M. A. Zidan, W. Ma, S. H. Lee, W. D. Lu, Reservoir computing using dynamic memristors for temporal information processing. *Nat. Commun.* **8**, 2204 (2017).
17. J. Moon, W. Ma, J. H. Shin, F. Cai, C. Du, S. H. Lee, W. D. Lu, Temporal data classification and forecasting using a memristor-based reservoir computing system. *Nat. Electron.* **2**, 480–487 (2019).
18. R. Midya, Z. Wang, S. Asapu, X. Zhang, M. Rao, W. Song, Y. Zhuo, N. Upadhyay, Q. Xia, J. J. Yang, Reservoir computing using diffusive memristors. *Adv. Intell. Syst.* **1**, 1900084 (2019).
19. X. Zhu, Q. Wang, W. D. Lu, Memristor networks for real-time neural activity analysis. *Nat. Commun.* **11**, 2439 (2020).
20. L. Sun, Z. Wang, J. Jiang, Y. Kim, B. Joo, S. Zheng, S. Lee, W. J. Yu, B. S. Kong, H. Yang, In-sensor reservoir computing for language learning via two-dimensional memristors. *Sci. Adv.* **7**, eabg1455 (2021).
21. Y. Zhong, J. Tang, X. Li, B. Gao, H. Qian, H. Wu, Dynamic memristor-based reservoir computing for high-efficiency temporal signal processing. *Nat. Commun.* **12**, 408 (2021).
22. J. Hochstetter, R. Zhu, A. Loeffler, A. Diaz-Alvarez, T. Nakayama, Z. Kuncic, Avalanches and edge-of-chaos learning in neuromorphic nanowire networks. *Nat. Commun.* **12**, 4008 (2021).
23. G. Milano, G. Pedretti, K. Montano, S. Ricci, S. Hashemkhani, L. Boarino, D. Ielmini, C. Ricciardi, In materia reservoir computing with a fully memristive architecture based on self-organizing nanowire networks. *Nat. Mater.* **21**, 195–202 (2022).
24. J. Nakayama, K. Kanno, A. Uchida, Laser dynamical reservoir computing with consistency: An approach of a chaos mask signal. *Opt. Express* **24**, 8679–8692 (2016).
25. C. G. Langton, Computation at the edge of chaos: Phase transitions and emergent computation. *Phys. D Nonlinear Phenomena* **42**, 12–37 (1990).
26. T. Tsuchiya, K. Terabe, M. Aono, All-solid-state electric-double-layer transistor based on oxide ion migration in Gd-doped CeO_2 on $SrTiO_3$ single crystal. *Appl. Phys. Lett.* **103**, 073110 (2013).
27. T. Tsuchiya, K. Terabe, M. Aono, In situ and non-volatile bandgap tuning of multilayer graphene oxide in an all-solid-state electric double-layer transistor. *Adv. Mater.* **26**, 1087–1091 (2014).
28. T. Tsuchiya, S. Moriyama, K. Terabe, M. Aono, Modulation of superconducting critical temperature in niobium film by using all-solid-state electric-double-layer transistor. *Appl. Phys. Lett.* **107**, 013104 (2015).
29. T. Tsuchiya, M. Ochi, T. Higuchi, K. Terabe, M. Aono, Effect of ionic conductivity on response speed of $SrTiO_3$-based all-solid-state electric-double-layer transistor. *ACS Appl. Mater. Interfaces* **7**, 12254–12260 (2015).
30. K. Terabe, T. Tsuchiya, R. Yang, M. Aono, Nanoionic devices enabling a multitude of new features. *Nanoscale* **8**, 13873–13879 (2016).
31. K. Terabe, T. Tsuchiya, T. Tsuruoka, A variety of functional devices realized by ionic nanoarchitectonics, complementing electronics components. *Adv. Electron. Mater.* **8**, 2100645 (2021).
32. K. Terabe, T. Tsuchiya, T. Tsuruoka, Solid state ionics for the development of artificial intelligence components. *Jpn. J. Appl. Phys.* **61**, SM0803 (2022).
33. T. Tsuchiya, M. Takayanagi, K. Mitsuishi, M. Imura, S. Ueda, Y. Koide, T. Higuchi, K. Terabe, The electric double layer effect and its strong suppression at Li^+ solid electrolyte/hydrogenated diamond interfaces. *Commun. Chem.* **4**, 117 (2021).
34. M. Akai-Kasaya, Y. Takeshima, S. Kan, K. Nakajima, T. Oya, T. Asai, Performance of reservoir computing in a random network of single-walled carbon nanotubes complexed with polyoxometalate. *Neuromorph. Comput. Eng.* **2**, 014003 (2022).
35. L. Appeltant, M. C. Soriano, G. Van der Sande, J. Danckaert, S. Massar, J. Dambre, B. Schrauwen, C. R. Mirasso, I. Fischer, Information processing using a single dynamical node as complex system. *Nat. Commun.* **2**, 468 (2011).
36. S. Kan, K. Nakajima, T. Asai, M. Akai-Kasaya, Physical implementation of reservoir computing through electrochemical reaction. *Adv. Sci.* **9**, 2104076 (2022).
37. S. Kan, K. Nakajima, Y. Takeshima, T. Asai, Y. Kuwahara, M. Akai-Kasaya, Simple reservoir computing capitalizing on the nonlinear response of materials: Theory and physical implementations. *Phys. Rev. Appl.* **15**, 024030 (2021).
38. J. Boedecker, O. Obst, J. T. Lizier, N. M. Mayer, M. Asada, Information processing in echo state networks at the edge of chaos. *Theory Biosci.* **131**, 205–213 (2012).
39. K. Fukuda, Y. Horio, Analysis of dynamics in chaotic neural network reservoirs: Time-series prediction tasks. *Nonlinear Theory Appl. IEICE* **12**, 639–661 (2021).
40. D. Snyder, A. Goudarzi, C. Teuscher, Computational capabilities of random automata networks for reservoir computing. *Phys. Rev. E* **87**, 042808 (2013).
41. A. L. Hodgkin, A. F. Huxley, A quantitative description of membrane current and its application to conduction and excitation in nerve. *J. Physiol.* **117**, 500–544 (1952).
42. C. E. Stafstrom, P. C. Schwindt, M. C. Chubb, W. E. Crill, Properties of persistent sodium conductance and calcium conductance of layer V neurons from cat sensorimotor cortex in vitro. *J. Neurophysiol.* **53**, 153–170 (1985).
43. S. G. Koh, H. Shima, Y. Naitoh, H. Akinaga, K. Kinoshita, Reservoir computing with dielectric relaxation at an electrode–Ionic liquid interface. *Sci. Rep.* **12**, 6958 (2022).
44. Y. LeCun, L. Bottou, Y. Bengio, P. Haffner, Gradient-based learning applied to document recognition. *Proc. IEEE* **86**, 2278–2324 (1998).
45. A. F. Atiya, A. G. Parlos, New results on recurrent network training: Unifying the algorithms and accelerating convergence. *IEEE Trans. Neural Netw.* **11**, 697–709 (2000).
46. Z. Siroma, N. Fujiwara, S. I. Yamazaki, M. Asahi, T. Nagai, T. Ioroi, Mathematical solutions of comprehensive variations of a transmission-line model of the theoretical impedance of porous electrodes. *Electrochim. Acta* **160**, 313–322 (2015).
47. M. Inubushi, K. Yoshimura, Reservoir computing beyond memory-nonlinearity trade-off. *Sci. Rep.* **7**, 10199 (2017).
48. M. Sano, Y. Sawada, Measurement of the Lyapunov spectrum from a chaotic time series. *Phys. Rev. Lett.* **55**, 1082–1085 (1985).

49. S. Kumar, J. P. Strachan, R. S. Williams, Chaotic dynamics in nanoscale NbO_2 Mott memristors for analogue computing. *Nature* **548**, 318–321 (2017).
50. N. Bertschinger, T. Natschläger, Real-time computation at the edge of chaos in recurrent neural networks. *Neural Comput.* **16**, 1413–1436 (2004).
51. H. Ardebili, J. Zhang, M. G. Pecht, *Encapsulation Technologies for Electronic Applications* (Elsevier, 2018).
52. A. Chakrabarti, S. Biswas, A. Prabhakar, E. Bhattacharya, Equation based modeling of MOSFET, in *Excerpt from the Proceedings of the COMSOL Conference* (2019).https://www.comsol.jp/paper/download/682661/Bangalore_2019_Poster_AnweshanChakravarty.pdf
53. S. Subramaniyam, S. Muthusamy, S. K. Bharatan, Simulation of molybdenum disulfide based MOSFET device using COMSOL multiphysics software. *J. Phys. Conf. Ser.* **2312**, 012057 (2022).
54. M. W. Verbrugge, P. Liu, Microstructural analysis and mathematical modeling of electric double-layer supercapacitors. *J. Electrochem. Soc.* **152**, D79 (2005).
55. G. Zhang, Simulating the electrical double layer capacitance, in *Excerpt from the Proceedings of the COMSOL Conference* (2010).https://www.comsol.jp/paper/download/101189/zhang_paper.pdf
56. "Parasitic Reactions in an Electrochemical Capacitor" COMSOL, Application Gallery; www.comsol.jp/model/download/907051/models.battery.electrochemical_capacitor_side_reactions.pdf.
57. N. Kuwata, X. Lu, T. Miyazaki, Y. Iwai, T. Tanabe, J. Kawamura, Lithium diffusion coefficient in amorphous lithium phosphate thin films measured by secondary ion mass spectroscopy with isotope exchange methods. *Solid State Ion.* **294**, 59–66 (2016).
58. H. Kawarada, Hydrogen-terminated diamond surfaces and interfaces. *Sur. Sci. Rep.* **26**, 205–206 (1996).
59. K. Kimura, K. Nakajima, S. Yamanaka, M. Hasegawa, Hydrogen depth-profiling in chemical-vapor-deposited diamond films by high-resolution elastic recoil detection. *Appl. Phys. Lett.* **78**, 1679–1681 (2001).
60. J. Dambre, D. Verstraeten, B. Schrauwen, S. Massar, Information processing capacity of dynamical systems. *Sci. Rep.* **2**, 514 (2012).

Acknowledgments

Funding: This work was supported by the Japan Society for the Promotion of Science (JSPS) KAKENHI grant number JP22H04625 (Grant-in-Aid for Scientific Research on Innovative Areas "Interface Ionics"), Japan Society for the Promotion of Science (JSPS) KAKENHI grant number JP21J21982 (Grant-in-Aid for JSPS Fellows), and Yazaki Memorial Foundation for Science and Technology Kurata grants from The Hitachi Global Foundation. **Author contributions:** T.T., D.N., W.N., and K.T. conceived the idea for the study. D.N., T.T., and W.N. designed the experiments. D.N. and T.T. wrote the paper. D.N. and W.N. carried out the experiments. D.N., W.N., and M.T. prepared the samples. D.N., T.T., and W.N. analyzed the data. D.N. carried out the multiphysics calculations. All authors discussed the results and commented on the manuscript. K.T. directed the projects. **Competing interests:** Pending patent (JP2022-009030): Patent application form was submitted to Japan Patent Office. Authors of the patent are T.T., D.N., W.N., M.T., and K.T. The authors declare that they have no other competing interests. **Data and materials availability:** All data needed to evaluate the conclusions in the paper are present in the paper and/or the Supplementary Materials.

Submitted 26 July 2022
Accepted 14 November 2022
Published 14 December 2022
10.1126/sciadv.ade1156